A *CHANDRA* STUDY OF THE LARGE-SCALE SHOCK AND COOL FILAMENTS IN HYDRA A: EVIDENCE FOR SUBSTANTIAL GAS DREDGE-UP BY THE CENTRAL OUTBURST

Myriam Gitti[1,2], Paul E. J. Nulsen[1], Laurence P. David[1], Brian R. McNamara[1,3,4], and Michael W. Wise[5]

[1] Harvard-Smithsonian Center for Astrophysics, 60 Garden Street, Cambridge, MA 02138, USA
[2] Astronomical Observatory of Bologna, INAF, via Ranzani 1, I-40127 Bologna, Italy
[3] Department of Physics & Astronomy, University of Waterloo, 200 University Avenue West, Waterloo, Ontario N2L 2G1, Canada
[4] Perimeter Institute for Theoretical Physics, Waterloo, Canada
[5] ASTRON Netherlands Institute for Radio Astronomy, P.O. Box 2, 7990 AA Dwingeloo, The Netherlands

ABSTRACT

We present the results of a *Chandra* study of the Hydra A galaxy cluster, where a powerful active galactic nucleus (AGN) outburst created a large-scale cocoon shock. We investigated possible azimuthal variations in shock strength and shape, finding indications for a weak shock with a Mach number in the range $\sim$1.2–1.3. We measured the temperature change across the shock front. However, the detection of a temperature rise in the regions immediately inside of the front is complicated by the underlying temperature profile of the cluster atmosphere. We measured the global temperature profile of the cluster up to 700 kpc, which represents the farthest measurement obtained with *Chandra* for this cluster. A "plateau" in the temperature profile in the range $\sim$70–150 kpc indicates the presence of cool gas, which is likely the result of uplift of material by the AGN outburst. After masking the cool filaments visible in the hardness ratio map, the plateau disappears and the temperature profile recovers a typical shape with a peak around 190 kpc, just inside the shock front. However, it is unlikely that such a temperature feature is produced by the shock as it is consistent with the general shape of the temperature profiles observed for relaxed galaxy clusters. We studied the spectral properties of the cool filaments finding evidence that $\sim 10^{11} M_\odot$ of low-entropy material has been dredged up by the rising lobes from the central 30 kpc to the observed current position of 75–150 kpc. The energy required to lift the cool gas is $\gtrsim 2.2 \times 10^{60}$ erg, which is comparable to the work required to inflate the cavities and is $\sim$25% of the total energy of the large-scale shock. Our results show that the AGN feedback in Hydra A is acting not only by directly heating the gas, but also by removing a substantial amount of potential fuel for the supermassive black hole.

Key words: galaxies: active – galaxies: clusters: general – galaxies: clusters: individual (Hydra A) – galaxies: clusters: intracluster medium – X-rays: galaxies: clusters

Online-only material: color figures

1. INTRODUCTION

Observational and theoretical evidence has been growing in the past decade in favor of the existence in galaxy clusters of a feedback mechanism that prevents cool cores from establishing "cooling flows" at the rates predicted by earlier X-ray observations (e.g., see Peterson & Fabian 2006 for a review). The dominant cD galaxies, which are present at the cluster center in all cool core clusters, host the most massive black holes in the local universe and usually show nuclear activity. They accordingly provide a natural feedback mechanism for the regulation of the cooling process. Feedback is also required to suppress the overproduction of massive galaxies predicted by dark-matter-only simulations and to break the self-similarity of clusters (e.g., Benson et al. 2003). The nature of this feedback, vital to our understanding of galaxy and structure evolution, is one of the most important unresolved questions in extragalactic astronomy. Based on the detection of cavities and active galactic nucleus (AGN)-driven shocks, the primary source of feedback in cluster has been identified as radio galaxies acting through outbursts and accompanying energy injection, likely intermittent, from the central AGN (e.g., for a review, see McNamara & Nulsen 2007 and references therein). In galaxy clusters, where cooling rates should be highest, the current generation of X-ray observatories *Chandra* and *XMM-Newton* have shown that there is not a significant amount of gas cooling below about one-third of its virial temperature (Peterson et al. 2003; Kaastra

et al. 2004). Images from these telescopes also reveal highly disturbed structures in the cores of many clusters, including shocks, cavities, and sharp density discontinuities. At radio wavelengths, it is clear that AGN jets are the cause of many of these disturbances. The incidence and variety of bubbles, cavities, shocks, and ripples observed both in the radio and in X-rays in galaxy clusters provide direct evidence of the widespread presence of AGN-driven phenomena (see, e.g., Fabian et al. 2003 for a discussion of the Perseus cluster properties in terms of AGN-generated viscously damped sound waves; Nulsen et al. 2005 for shock heating in Hydra A; Gitti et al. 2007 for a study of giant cavities created by the most powerful AGN outburst currently known; Bîrzan et al. 2008 and Diehl et al. 2008 for a survey of cavities and the implied cavity heating rates). Such AGN feedback has a wide range of impacts, from the formation of galaxies, to the explanation of the observed $M_{\rm bh}$–σ relation (which indicates a causal connection or feedback mechanism between the formation of bulges and their central black holes, e.g., Magorrian et al. 1998), to the regulation of cool cores. In most cases, the energy introduced by the AGN is more than sufficient to counteract putative cooling flows (Bîrzan et al. 2004, 2008; Rafferty et al. 2006). However, the details of how the feedback loop operates are still unknown. Only by studying striking examples of interaction between the central radio galaxy and the intracluster medium (ICM) can we understand why cooling and star formation still proceeds at a reduced rate, and this is likely to reveal the coupling between AGN feedback and the ICM.

The galaxy cluster Hydra A has a well-known, large-scale system of X-ray cavities embedded in a "cocoon" shock surrounding the central, powerful radio source (McNamara et al. 2000; Nulsen et al. 2005). It is considered one of the prototypes of cool core clusters with cavities, which has served as an early test of the AGN feedback paradigm, and it has been extensively studied both in the radio and X-rays (Taylor et al. 1990; McNamara et al. 2000; David et al. 2001; Nulsen et al. 2002, 2005; Lane et al. 2004; Wise et al. 2007; Simionescu et al. 2009a, 2009b; Kirkpatrick et al. 2009). By analyzing the archival ∼200 ks *Chandra* exposure in this paper, we study the azimuthal properties of the large-scale shock and attempt to measure the temperature jump associated with the shock in different directions. We also perform a detailed spectral analysis of the cool X-ray filaments extending out to 150 kpc, finding evidence for extensive mass dredge-up from the central 30 kpc, which affects the global temperature profile of the cluster.

With $H_0 = 70$ km s^{-1} Mpc^{-1} and $\Omega_M = 1 - \Omega_\Lambda = 0.3$, the luminosity distance to Hydra A ($z = 0.0538$) is 240 Mpc and $1''$ corresponds to 1.05 kpc in the rest frame of the cluster.

2. *CHANDRA* OBSERVATIONS AND DATA REDUCTION

Hydra A has been imaged four times by *Chandra* ACIS for a total exposure of 240 ks. The two shorter exposures (ObsIDs 575 and 576, which collectively comprise only ∼17% of the total exposure) were taken early in the *Chandra* mission when the ACIS detector was operated at the higher focal plane temperature of −110 °C. Due to the higher quality calibration at −120 °C, the spectral analysis presented below was performed on the two longer, more recent exposures: ∼97 ks collected on 2004 January 13 (ObsID 4969) and ∼99 ks collected on 2004 October 22 (ObsID 4970) with ACIS-S. We use data from the S3 and S2 CCDs to study the central part of the cluster emission, where the cavity system and the radio source are located, and from the I2 and I3 CCDs to measure the temperature and surface brightness in the cluster outskirts. Each data set was individually reprocessed with CIAO version 4.1 using CALDB 4.1.0 and corrected for known time-dependent gain and charge transfer inefficiency problems following techniques similar to those described in the *Chandra* analysis threads.[6] Screening of the event files was also applied to filter out strong background flares. Blank-sky background files, filtered in the same manner as in the Hydra A image and normalized to the count rate of the source image in the 10–12 keV band, were used for background subtraction. We identified and removed the point sources using the CIAO task WAVDETECT, with the detection threshold set to the default value of 10^{-6}. The final, combined exposure time for the two data set is 174.2 ks.

3. THE LARGE-SCALE SHOCK

The observed feature interpreted as a shock front in the X-ray surface brightness of Hydra A surrounds the low-frequency radio lobes, and the correspondence between their shapes supports the interpretation of a cocoon shock of the radio source. Nulsen et al. (2005) estimated an age of the outburst to be $t_s = 1.4 \times 10^8$ yr with a total energy of $E_s = 9 \times 10^{60}$ erg. The shock front is clearly aspherical with a complicated three-dimensional shape affected by projection effects. In particular, the Hydra A radio source and cavity system is inclined at about 40° to the plane of the sky, with the northern side lying

---

[6] http://cxc.harvard.edu/ciao/threads/index.html
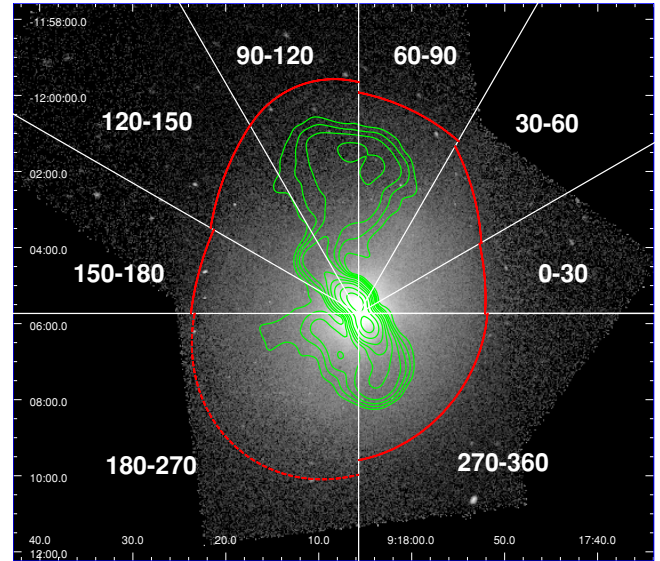
Figure 1. Residual map of the beta model subtracted surface brightness image from Nulsen et al. (2005). The green contours outline the 330 MHz radio emission from Lane et al. (2004). Overlaid in white are the sectors considered in the investigation of the azimuthal variations in shock properties by means of the surface brightness profile. In each sector, the red curve indicates the position of the shock front determined by fitting a broken power-law density model to the surface brightness profile (see Figure 2 and Section 3.1 for details). In sector 180–270, where the surface brightness discontinuity is least evident, we have indicated the shock front with a dashed curve.

(A color version of this figure is available in the online journal.)

closer to us (Taylor 1996; Lane et al. 2004; Wise et al. 2007). The cavity and shock geometry as well as the outburst history and energetics have been studied in detail in Wise et al. (2007) and Simionescu et al. (2009a).

3.1. Azimuthal Variations in Shock Strength

We have investigated the azimuthal variations in shock strength and shape by studying surface brightness profiles in different directions. In particular, we have divided the northern cluster semicircle into six sectors of 30° each, and the southern cluster semicircle, where the shock is less evident in the image, into two quadrants of 90° each. Starting from the west with position angle (P.A.) = 0° and counting counterclockwise, the sectors are labeled as 0–30, 30–60, 60–90, 90–120, 120–150, 150–180, 180–270, and 270–360 (see Figure 1). We extracted the background-subtracted, exposure-corrected surface brightness profile along each sector in the energy range 0.5–2.0 keV. The center of the annular regions used to extract each profile was chosen in order to best match the curvature of the radial bins with the shape of the shock front as seen in the image (Figure 1). We then performed fits of a broken power-law density model to each surface brightness profile. This analysis assumes that the radius of curvature in the plane of the sky is the same as that parallel to the line of sight. A hydrodynamic model for the shock was made by initiating an explosion at the center of a hydrostatic, isothermal atmosphere with a power-law density profile (see Nulsen et al. 2005 for more details on the shock model). The power-law index for the density profile of the unshocked gas was determined from the broken power-law fit to the surface brightness profile. The surface brightness profiles and the best fits of broken power-law density models in the various sectors are shown in Figure 2, where the radial axes indicate the distance from the center of curvature of the annular
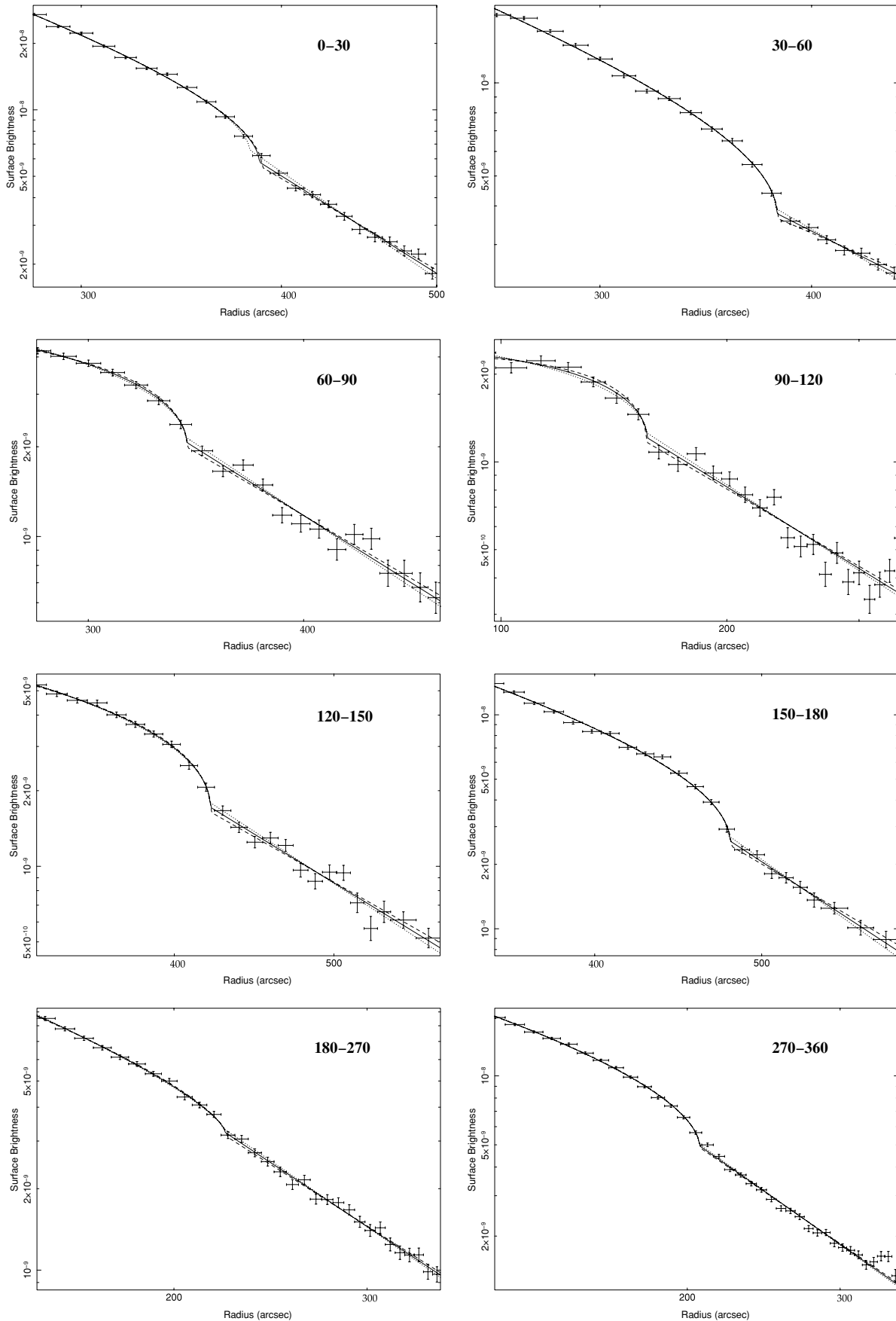
Figure 2. Background-subtracted, exposure-corrected *Chandra* surface brightness profiles extracted along the sectors outlined in Figure 1. The surface brightness is in units of counts cm^{-2} s^{-1}, with errors at 1σ. The radial axis shows the distance from the center of curvature of the annuli used to extract the surface brightness profile. Radial error bars show the bin sizes. The smooth curves show fits of the broken power-law density model which give the density jumps and corresponding Mach numbers reported in Table 1.

Table 1
Shock Properties

Sector $\theta_1-\theta_2$ (°)	Shock Radius $R_{\bar{\theta}}$ ('')	Radius Variation $R_{\theta_1}-R_{\theta_2}$ ('')	Density Jump	Mach Number $\mathcal{M}$
0–30	208	201–222	1.33	1.22
30–60	257	222–303	1.45	1.30
60–90	332	314–349	1.33	1.23
90–120	371	364–342	1.38	1.26
120–150	301	342–271	1.46	1.32
150–180	260	264–265	1.40	1.27
180–270	285	260–253	1.15	1.10
270–360	205	233–202	1.35	1.23

Notes. Results of the fits of a broken power-law density model to the surface brightness profiles extracted along different sectors. The sector aperture (from P.A. θ_1 to θ_2) is indicated in the first column. The shock radius at the mid-angle of the sector ($R_{\bar{\theta}}$) is indicated in the second column, whereas the shock radii at the starting (R_{θ_1}) and ending (R_{θ_1}) angles are indicated in the third column. Such radial distances are measured from the cluster center. The corresponding density jump and Mach number ($\mathcal{M}$) are shown in the fourth and fifth columns, respectively. Best-fit statistical errors are on average ~5%.

regions used to extract the profiles. However, in the following discussion we indicate the position of the shock in each sector (referred to as the "shock radius") in terms of the distance of the front at mid-aperture of the sector from the cluster center. The best-fit model for each sector is summarized in Table 1 and the corresponding shock front is shown by red arcs in Figure 1. We also investigated the effects of varying the radial binning and center of curvature of the annular regions used to extract the profile. We found that the fit results (i.e., shock radius and Mach number, $\mathcal{M}$) do not depend strongly on the particular choice of the extraction region nor on the radial range of the fit, with systematic variations $\lesssim 5\%$ in each sector.

The shock is clearly visible as a surface brightness jump in all sectors but the 180–270 sector (i.e., the southeast (SE) quadrant), with a radius varying between ~205'' in the east–west direction and ~365'' in the north–south direction. The Mach number varies between 1.20 and 1.32 in the sectors where the density jump is detected, whereas to the southeast (sector 180–270) where the surface brightness discontinuity is less evident we estimate $\mathcal{M} = 1.10$. These results are consistent with Nulsen et al. (2005), and partially in agreement with Simionescu et al. (2009a), who report a detection of the shock front also in the south direction.

3.2. Temperature Variations Across the Shock Front

Our shock model predicts the emission-weighted temperature to rise across the front by ~8%, 10%, 15%, and 20% for Mach numbers of 1.18, 1.23, 1.33, and 1.40, respectively, reaching its peak at a distance of ~5%–10% of the shock radius behind the shock and declining below the unshocked temperature values inside radial distances of ~25% of the shock radius. We used this information to optimize our selection of the pre-shock and post-shock regions in each sector and then extracted the spectra in these regions using the SPECEXTRACT task, which also computes the corresponding event-weighted response matrices. Spectral fitting to a single absorbed apec model was performed in XSPEC version 12.3.1 in the 0.5–8.0 keV energy range. Abundances were measured relative to the abundances of Anders & Grevesse (1989) and a galactic hydrogen column of 4.68×10^{20} cm^{-2} (Dickey & Lockman 1990) was assumed. As a general result, the post-shock regions are found to be hotter than the corresponding pre-shock regions, although due

Table 2
Temperature Profile Derived by Spectral Fitting

Bin No.	Radius ('')	kT (keV)	χ^2/dof	kT_{mask} (keV)	χ^2/dof
1	0–13	$2.93^{+0.04}_{-0.04}$	763/560	$3.11^{+0.07}_{-0.07}$	453/430
2	13–21	$3.07^{+0.04}_{-0.04}$	638/590	$3.26^{+0.06}_{-0.06}$	520/466
3	21–29	$3.29^{+0.04}_{-0.04}$	607/598	$3.34^{+0.05}_{-0.05}$	589/566
4	29–37	$3.39^{+0.05}_{-0.05}$	663/600	$3.55^{+0.07}_{-0.07}$	628/565
5	37–46	$3.61^{+0.06}_{-0.06}$	681/622	$3.76^{+0.07}_{-0.07}$	605/584
6	46–58	$3.60^{+0.06}_{-0.06}$	644/607	$3.73^{+0.07}_{-0.07}$	615/578
7	58–72	$3.62^{+0.07}_{-0.06}$	737/623	$3.81^{+0.07}_{-0.07}$	618/593
8	72–89	$3.51^{+0.07}_{-0.07}$	656/627	$3.73^{+0.10}_{-0.10}$	512/502
9	89–107	$3.51^{+0.07}_{-0.07}$	748/629	$3.85^{+0.10}_{-0.10}$	538/513
10	107–126	$3.52^{+0.07}_{-0.07}$	698/634	$3.82^{+0.10}_{-0.10}$	507/508
11	126–145	$3.58^{+0.07}_{-0.07}$	713/648	$3.78^{+0.11}_{-0.11}$	491/511
12	145–168	$3.79^{+0.07}_{-0.07}$	744/674	$3.91^{+0.08}_{-0.08}$	672/643
13	168–201	$4.02^{+0.08}_{-0.08}$	719/709	$4.02^{+0.08}_{-0.08}$	719/709
14	201–257	$3.91^{+0.08}_{-0.08}$	1125/1124	$3.91^{+0.08}_{-0.08}$	1125/1124
15	257–339	$3.70^{+0.11}_{-0.11}$	1252/1177	$3.70^{+0.11}_{-0.11}$	1252/1177
16	339–497	$3.58^{+0.19}_{-0.19}$	1140/1150	$3.58^{+0.19}_{-0.19}$	1140/1150
17	497–812	$2.96^{+0.30}_{-0.29}$	1717/1676	$2.96^{+0.30}_{-0.29}$	1717/1676

Notes. Results of the spectral fitting in concentric 360° annular regions (shown in Figure 3) in the 0.5–8.0 keV energy range using the XSPEC wabs×apec model. The absorbing column density is fixed to the Galactic value ($N_{\text{H}} = 4.68 \times 10^{20}$ cm^{-2}), while the temperature (in keV) and metallicity (not reported here) are left as free parameters. Error bars are at the 90% confidence levels on a single parameter of interest. The values of kT_{mask} are measured in the same concentric annular regions after excluding the cool filaments (i.e., by fitting spectra extracted after masking the blue sectors shown in Figure 5, left panel). See Section 4 for details.

to the large error bars the temperature of the pre-shock and post-shock gas is consistent. Some examples of these temperature measurements are presented in Section 6.1. A further attempt to bin sectors together in order to increase the statistics did not lead to any clear detections of a temperature jump across the shock front (see Section 6.1). However, previous measurements (David et al. 2001; Simionescu et al. 2009a) indicate that the underlying global temperature profile has a peak close to the inner edge of the shock front, thus complicating the detection of a temperature rise due to the shock itself. To investigate this in more detail, we study the properties of the azimuthally averaged cluster temperature profile in Section 4.

4. GLOBAL CLUSTER TEMPERATURE PROFILE

The azimuthally averaged gas temperature profile was derived from the ACIS-S and ACIS-I data by extracting spectra in the annular regions indicated in Figure 3, and is shown in the left panel of Figure 4. The annular bins and temperature measurements are detailed in Table 2. The two outer temperature points represent the farthest temperature measurements from the cluster center obtained with *Chandra* data at present. We note that the temperature profile peaks around 180'', just inside the inner edge of the shock front. However, as discussed in Section 6, it is unlikely that this temperature feature is produced by the shock as it is consistent with the general shape of temperature profiles observed for relaxed galaxy clusters.

On the other hand, a "plateau" is notable in the temperature profile indicating the presence of cool gas in the
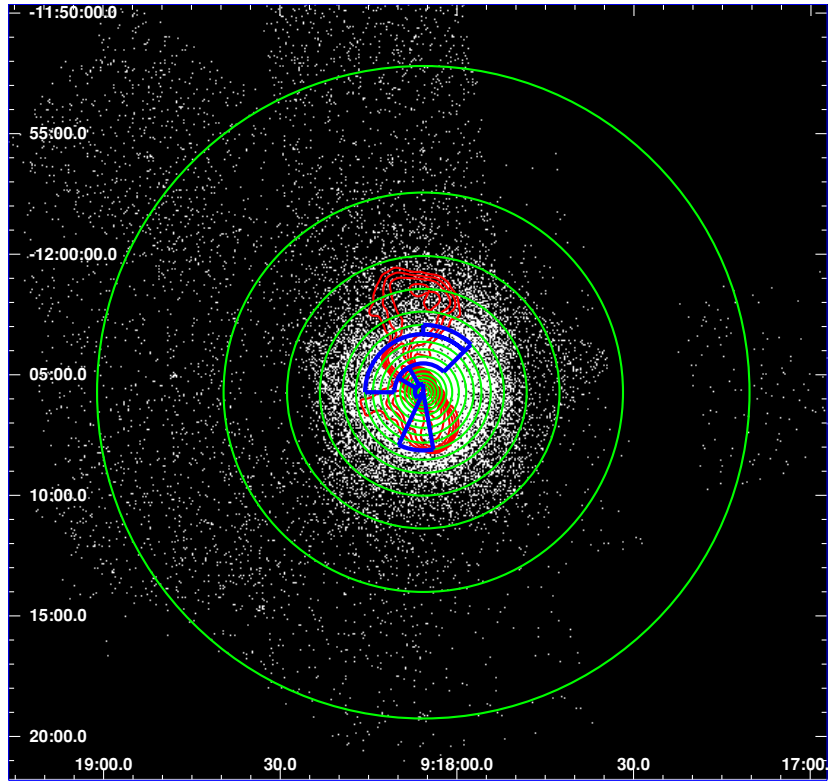
Figure 3. *Chandra* 0.5–7.0 keV mosaic of the Hydra A field from Wise et al. (2007). Overlaid in green are the annuli used to measure the azimuthally averaged temperature profile shown in the left panel of Figure 4. The blue sectors indicate the regions where the cool filament is present. These sectors have been excluded in determining the temperature profile shown in the right panel of Figure 4 (see Section 5 for details). The red contours outlining the 330 MHz radio emission from Lane et al. (2004) are also shown for comparison.

(A color version of this figure is available in the online journal.)
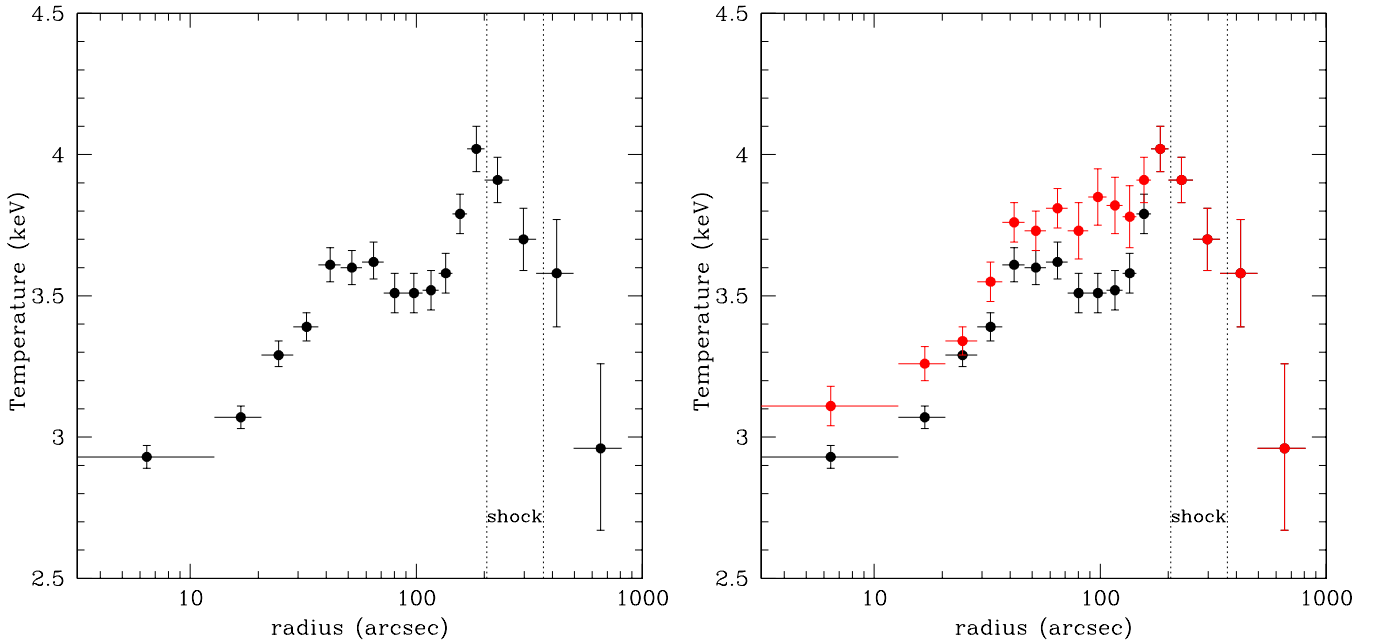
Figure 4. Left: azimuthally averaged gas temperature profile derived from the ACIS-S and ACIS-I data by fitting spectra in the annuli shown in Figure 3. The dotted lines indicate the inner and outer radii of the shock front as determined in Section 3.1. Right: same as left panel, with the profile measured after excluding the cool filaments (i.e., after excluding the blue sectors shown in Figure 5, left panel) overlaid in red.

(A color version of this figure is available in the online journal.)

range of radius ∼70″–150″. This peculiar feature has not been noted previously in the literature. We thus investigated it in more detail thanks to the deep, high-quality *Chandra* exposure.

4.1. Evidence for Cool Filaments

In order to investigate the origin of the plateau seen in the temperature profile between ∼70″ and 150″, we made several
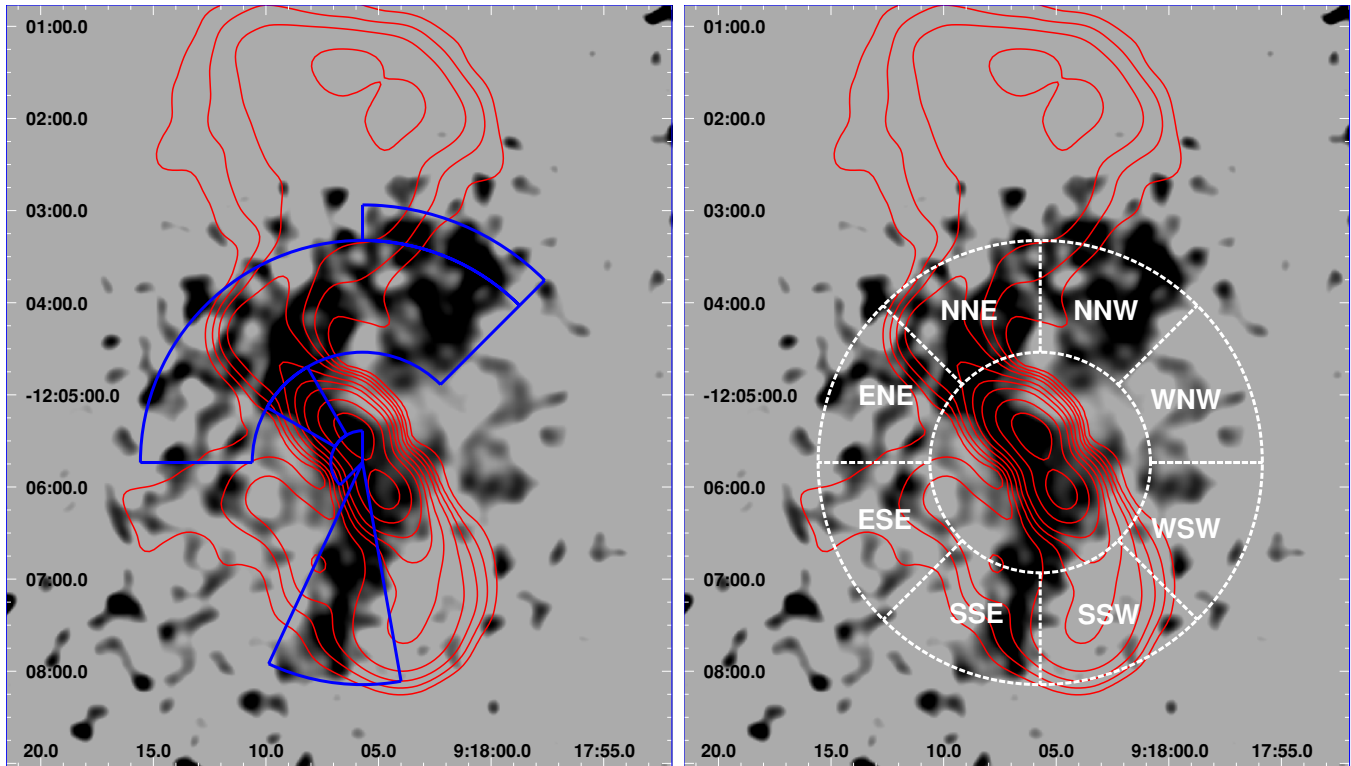
Figure 5. Left: high-contrast hardness ratio map obtained by dividing a 1.5–7.5 keV image by a 0.3–1.5 keV image. Each raw image was smoothed with a 10 pixel (5″) Gaussian before the division. The images were extracted from the merged cleaned event files for ObsIDs 4969 and 4970. Regions in black are indicative of low-temperature gas. The blue sectors indicate the selected regions of supposedly cool filaments. These regions have been excluded in measuring the temperature profile shown in the right panel of Figure 4 (red points). The red contours outlining the 330 MHz radio emission from Lane et al. (2004) are also shown for comparison. Right: similar to left panel. Overlaid in white are the sectors used to study the spectral properties of the cool filaments (located between radii 72″–145″ ∼ 76–152 kpc; see Section 5 for details).

(A color version of this figure is available in the online journal.)

attempts to identify regions of cool gas. Our approach was to measure a new, "undisturbed" temperature profile by masking such regions and then compare it with the global temperature profile measured above. We first masked the cavity regions (as indicated in Wise et al. 2007), finding systematically higher temperatures by ∼0.1–0.2 keV in all bins (except for the very central bin, where the temperature is lower by ∼0.15 keV) up to ∼200″. The temperature profile measured by masking the cavities is therefore shifted up, maintaining its global shape. In particular, the plateau in the temperature profile is still present, indicating that the cavities are not a tracer of the entire amount of cool gas. We then masked the ∼1′ bright filament stretching from the inner cavity to the center of a larger outer cavity in the northeast, which was noted by Nulsen et al. (2005). As in the previous attempt, the plateau in the temperature profile remained, indicating that the known filament is not the only repository of the cool gas in Hydra A.

As a diagnostic of the presence of cool gas we finally used the hardness ratio map shown in Figure 5, which was obtained by dividing a smoothed 1.5–7.5 keV image by a smoothed 0.3–1.5 keV image. The dark regions are indicative of low gas temperatures. They agree with the arm-like structures of cooler gas extending toward the north and the south in the temperature map of Simionescu et al. (2009b). Based on a visual inspection of the hardness ratio map, we selected a simple combination of sectors reproducing the shape of the supposedly cool filaments (see the left panel of Figure 5). We then excluded these regions and extracted the spectra in the same radial bins as above (see

Figure 3), and generated the temperature profile shown in red in the right panel of Figure 4 (see Table 2). As evident from the comparison of the two profiles, the plateau has largely been removed and the temperature profile is typical of cool core clusters (see also Section 6). This clearly indicates that the masked regions contain cool gas. A detailed spectral analysis of the cool filaments is presented in Section 5.

5. SPECTRAL PROPERTIES OF THE COOL GAS

We investigate here the spectral properties of the gas which produces the plateau seen in the global cluster temperature profile. In particular, we focus on the gas located in the range of projected distances from the center of 72″–145″ (∼76–152 kpc), which corresponds to the radial range where the plateau in the temperature profile is most evident (i.e., bin numbers 8–11; see Figure 4 and Table 2). We divided the annulus from 72″–145″ into eight sectors, each having an angular width of 45°, obtaining the regions labeled as WNW (west–northwest), NNW (north–northwest), NNE (north–northeast), ENE (east–northeast), ESE (east–southeast), SSE (south–southeast), SSW (south–southwest), and WSW (west–southwest) in the right panel of Figure 5. We extracted the spectra in these sectors and compared two different spectral models. The "1T model" is the absorbed `apec` model already used above to derive the global temperature profile. The free parameters are the temperature, kT, the metallicity, Z, and the normalization (emission measure, EM). The "2T model" includes a second thermal emission component (`apec+apec`) and
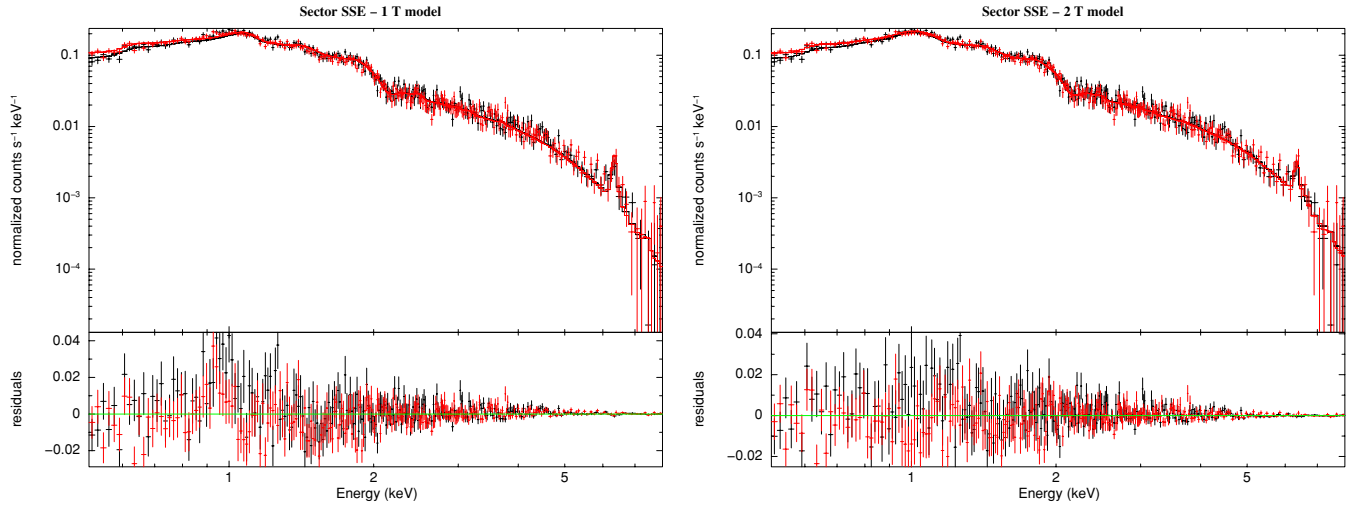
Figure 6. 1T model (left) and 2T model (right) fit to the spectra extracted in the SSE sector. See Table 3 for best-fitting parameter values.

(A color version of this figure is available in the online journal.)

Table 3
Spectral Analysis of the Cool Filaments

| | 1T Model | | | | 2T Model | | | | | | |
Sector	kT (keV)	EM ($\times 10^{-3}$)	Z (solar)	χ^2/dof [χ^2_ν]	kT_1 (keV)	$EM_1(\times 10^{-3})$	kT_2(keV)	$EM_2(\times 10^{-3})$	Z (solar)	χ^2/dof	F stat
WNW	$3.87^{+0.10}_{-0.10}$	$1.60^{+0.03}_{-0.03}$	$0.37^{+0.05}_{-0.05}$	505.1/521 [0.97]	$2.17^{+0.48}_{-0.47}$	$0.73^{+0.28}_{-0.45}$	$6.40^{+1.89}_{-1.74}$	$0.94^{+0.43}_{-0.28}$	$0.28^{+0.06}_{-0.05}$	484.6/519	11.0
NNW	$3.24^{+0.06}_{-0.07}$	$1.79^{+0.03}_{-0.03}$	$0.36^{+0.04}_{-0.04}$	524.9/525 [1.00]	$2.05^{+0.17}_{-0.25}$	$1.08^{+0.24}_{-0.34}$	$6.74^{+4.01}_{-1.75}$	$0.80^{+0.31}_{-0.35}$	$0.26^{+0.04}_{-0.04}$	467.6/523	32.0
NNE	$3.14^{+0.08}_{-0.08}$	$1.23^{+0.03}_{-0.03}$	$0.41^{+0.05}_{-0.05}$	483.0/460 [1.05]	$2.12^{+0.23}_{-0.21}$	$0.81^{+0.06}_{-0.29}$	$6.84^{+1.48}_{-2.20}$	$0.48^{+0.26}_{-0.11}$	$0.30^{+0.05}_{-0.05}$	451.9/458	15.8
ENE	$3.32^{+0.08}_{-0.08}$	$1.15^{+0.02}_{-0.02}$	$0.42^{+0.06}_{-0.05}$	455.5/455 [1.00]	$2.24^{+0.37}_{-0.47}$	$0.72^{+0.20}_{-0.47}$	$6.84^{+4.62}_{-2.72}$	$0.48^{+0.50}_{-0.20}$	$0.34^{+0.06}_{-0.05}$	433.6/453	11.4
ESE	$3.45^{+0.10}_{-0.10}$	$1.36^{+0.03}_{-0.03}$	$0.37^{+0.05}_{-0.05}$	502.2/483 [1.04]	$2.16^{+0.86}_{-0.48}$	$0.48^{+0.89}_{-0.35}$	$4.49^{+14.9}_{-0.61}$	$0.92^{+0.33}_{-0.66}$	$0.32^{+0.05}_{-0.05}$	491.2/481	5.4
SSE	$3.34^{+0.07}_{-0.07}$	$1.45^{+0.03}_{-0.03}$	$0.38^{+0.05}_{-0.05}$	621.8/491 [1.27]	$1.59^{+0.11}_{-0.23}$	$0.44^{+0.18}_{-0.21}$	$4.92^{+0.97}_{-0.74}$	$1.05^{+0.17}_{-0.15}$	$0.28^{+0.06}_{-0.05}$	533.9/489	40.3
SSW	$4.01^{+0.12}_{-0.12}$	$1.18^{+0.02}_{-0.02}$	$0.35^{+0.06}_{-0.06}$	458.0/472 [0.97]	$2.39^{+0.65}_{-0.90}$	$0.67^{+0.17}_{-0.53}$	$8.60^{+4.98}_{-4.12}$	$0.58^{+0.50}_{-0.22}$	$0.28^{+0.07}_{-0.07}$	438.2/470	10.6
WSW	$3.92^{+0.11}_{-0.11}$	$1.37^{+0.03}_{-0.03}$	$0.31^{+0.06}_{-0.05}$	439.4/494 [0.89]	$2.93^{+0.33}_{-1.14}$	$1.17^{+0.07}_{-0.85}$	$54.4^{+/}_{-/}$	$0.36^{+0.12}_{-0.12}$	$0.25^{+0.06}_{-0.05}$	419.5/492	11.7

Notes. Results of 1T model and 2T model spectral fitting in the 0.5–8.0 keV energy range. The annular sectors of spectra extraction are indicated in the right panel of Figure 5. The normalizations (EMs) are in XSPEC units of $10^{-14}n_e n_p V/4\pi[D_A(1+z)]^2$. Errors are at the 90% confidence levels on a single parameter of interest. The last column shows the result of the F-test. See Section 5 for details.

has two additional free parameters: the temperature, kT_2, and the normalization, EM_2, of the second component (the metallicities of the two components are linked).

The best-fitting parameter values and 90% confidence ranges derived from the fits to the annular spectra in sectors are summarized in Table 3. Although the improvement of adding a second thermal component is formally significant according to the F-test, our results show that the quality of the data is not generally sufficient to demand a model more complex than the 1T model. In fact, in most sectors, the 1T model already produces a very good fit (reduced $\chi^2_\nu \sim 1$) and therefore a more complicated model appears unnecessary. We also note that the second thermal component is poorly constrained, with temperature errors $\gtrsim 25\%$ and up to 300%. Only in the SSE sector is the reduced chi squared of the 1T model unacceptable at 90% significance, and the statistical improvement obtained by introducing an additional emission component compared to the single-temperature model is the most significant according to the F-test. The improvement of the 2T model over the 1T model in this sector is also evident from the residuals of the fits in Figure 6. We can therefore conclude that, confirming the hardness ratio map (Figure 5, right panel), we find spectral evidence for multiphase gas in the SSE sector with a hot component at $4.92^{+0.97}_{-0.74}$ keV and a cool component at $1.59^{+0.11}_{-0.23}$ keV.

Assuming that the two spectral phases are in pressure equilibrium in the same volume, the ratio of the volumes they occupy is estimated as $V_1/V_2 = (EM_1/EM_2)\cdot(kT_1/kT_2)^2$, so the filling factor of the cool gas is ~ 0.04.

By contrast, we do not find clear spectral signatures of cool gas in the sectors NNW, NNE, and ENE, as expected from a visual inspection of the hardness ratio map. However, the lack of spectral evidence for multiphase gas could be due to the limitations of our data. Indeed, due to the relatively limited spectral resolution of *Chandra*, the detection of two different thermal components demands a significant temperature separation. The temperature difference required to have a marked effect on a single-phase thermal fit at the 90% confidence level is determined as follows. Using the response matrices, background, and numerical information of a real spectrum extracted in an arbitrary sector, we simulated spectra with two thermal components separated by ΔT around the best-fit value of the single-temperature fit to the real spectrum. We then fitted a single-temperature `apec` model to the mock two-temperature spectrum. We repeated this exercise, increasing the separation between the two temperature components until χ^2_ν exceeds the 90% confidence range. For comparison, we performed this procedure by starting from the real spectra in different sectors indicated in Figure 5 and found consistent results. An example
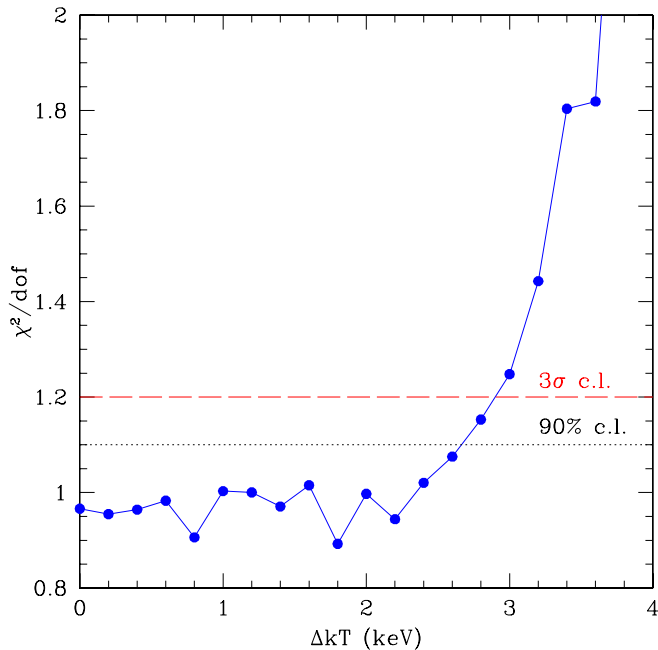
Figure 7. Reduced chi square of the 1T model fit to mock two-temperature spectra as a function of the separation ΔT of the two thermal components. The best-fit value of the single-temperature fit is $kT = 3.24 \pm 0.06$ keV.

(A color version of this figure is available in the online journal.)

Table 4
Spectral Analysis of the Cool Filaments

| Sector | 2T Model with $kT_2 = 4$ keV | | | | |
	kT_1 (keV)	$EM_1 (\times 10^{-3})$	$EM_2 (\times 10^{-3})$	χ^2/dof	F Statistics
WNW	$1.33^{+0.37}_{-0.24}$	$0.05^{+0.05}_{-0.04}$	$1.55^{+0.03}_{-0.04}$	493.8/520	11.9
NNW	$1.67^{+0.16}_{-0.11}$	$0.39^{+0.08}_{-0.07}$	$1.42^{+0.06}_{-0.07}$	478.8/524	50.5
NNE	$1.73^{+0.28}_{-0.08}$	$0.33^{+0.10}_{-0.05}$	$0.93^{+0.04}_{-0.10}$	456.9/459	26.2
ENE	$1.72^{+0.35}_{-0.13}$	$0.22^{+0.09}_{-0.05}$	$0.95^{+0.05}_{-0.09}$	436.6/454	19.7
ESE	$2.00^{+0.52}_{-0.35}$	$0.27^{+0.17}_{-0.09}$	$1.11^{+0.09}_{-0.17}$	492.5/482	9.5
SSE	$1.33^{+0.12}_{-0.08}$	$0.18^{+0.05}_{-0.04}$	$1.26^{+0.03}_{-0.03}$	539.1/490	75.2
SSW	$1.09^{+0.48}_{-0.26}$	$0.02^{+0.03}_{-0.01}$	$1.17^{+0.03}_{-0.02}$	451.4/471	6.9
WSW	$1.37^{+0.63}_{-0.35}$	$0.04^{+0.05}_{-0.03}$	$1.34^{+0.03}_{-0.04}$	433.1/493	7.2

Notes. Results of 2T model spectral fitting in the 0.5–8.0 keV energy range. The temperature value of the second thermal component is fixed to 4 keV. The annular sectors of spectra extraction are indicated in the right panel of Figure 5. The normalizations (EMs) are in XSPEC units of $10^{-14} n_e n_p V / 4\pi [D_A(1+z)]^2$. Errors are at the 90% confidence levels on a single parameter of interest. The last column shows the F statistic value testing the improvement of the 2T model over the 1T model in Table 3. See Section 5 for details.

of such an analysis is plotted in the left panel of Figure 7, where the dotted and dashed lines are the 90% and 3σ limits. We found that an ∼2.8 keV (3.0 keV) separation is necessary to exclude the presence of single-phase gas at the 90% (3σ) confidence for our data. The fact that the two spectral components detected in sector SSE are separated by ∼3.3 keV is consistent with this result. We note that kT_1 found by the 2T model fit in the SSE sector is the lowest among all of the sectors, falling in the energy range which comprises most of the counts and thus is more easily detectable.

Despite this, since a temperature higher than 4 keV is not observed at any radius in the cluster (Figure 4), the second thermal component found by the 2T model fit appears unrealistically hot, so we performed a new spectral fit with the 2T model (apec+apec) keeping the temperature of the second thermal component fixed at 4 keV. Such a model has only one additional free parameter than the 1T model: the normalization, EM_2, of the second component (the metallicities of the two components are linked). The best-fitting parameter values and 90% confidence levels derived from the fits to the annular spectra in sectors are summarized in Table 4. The F statistics for the improvement over the 1T model, shown in the last column, indicate where the addition of a second thermal component is most significant (sectors SSE, NNW, NNE, and ENE). In agreement with the hardness ratio map (Figure 5), our spectral analysis therefore supports the presence of multiphase gas along the filaments. Interestingly, such cool filaments follow the morphology of the powerful central radio source nicely, although the western part of the southern radio lobe appears devoid of cool gas. The SSW sector is indeed the hottest and is also the region where the presence of a second thermal component is least significant. This sector lies at the location where the southern radio lobe appears to fold back on itself (Lane et al. 2004). The properties of the cavity are also consistent with a sharp bend in the southern jet there (Wise et al. 2007).

Finally, we also attempted to map the EM distribution by fitting more complicated multiphase spectral models (such as apec+apec+apec+apec, with fixed temperatures and free normalizations). However, we found our data are inadequate due to limited statistics and the spectral resolution of *Chandra*. These detailed spectral studies will, hopefully, be possible in the future with the spectral capabilities of the *International X-ray Observatory* (*IXO*).

6. DISCUSSION

6.1. Scaled Temperature Profile and Shock Front

We show in the left panel of Figure 8 the observed temperature profile of Hydra A (red triangles), scaled by the virial radius (estimated from the relation $r_{vir} = 2.74\,\mathrm{Mpc}\sqrt{\langle T_X\rangle/10\,\mathrm{keV}}$; Evrard et al. 1996), overlaid on the scaled temperature profiles of a sample of 12 relaxed clusters observed with *Chandra* (Vikhlinin et al. 2005). The temperatures are scaled to the emission-weighted cluster temperature $\langle T_X\rangle$, measured after excluding the central 70 kpc region which is usually affected by radiative cooling. We note that the plateau of cool gas, already discussed in Section 4, stands out from to the typical temperature profile of clusters. In particular, lying just inside the typical temperature peak, such a plateau emphasizes the temperature peak in Hydra A, making it look higher than it actually is. Since this region is also where the shock front is located, it makes it difficult to distinguish between a temperature jump due to the shock and the typical temperature peak of the cluster.

In fact, once we overlay the scaled temperature profile of Hydra A measured after masking the cool filaments (right panel of Figure 4) it is remarkable how well it agrees with the general shape of the temperature profiles observed for relaxed clusters (see the right panel of Figure 8). Therefore, it is unlikely that the temperature peak observed in Hydra A is produced by the shock. In particular, the spectroscopic detection of a temperature rise in the regions immediately inside of the shock front is complicated by the underlying rising temperature profile of the global cluster atmosphere. In Figure 9, we show some examples of such temperature measurements in various sectors (see Section 3.2): the post-shock regions are found to be hotter than
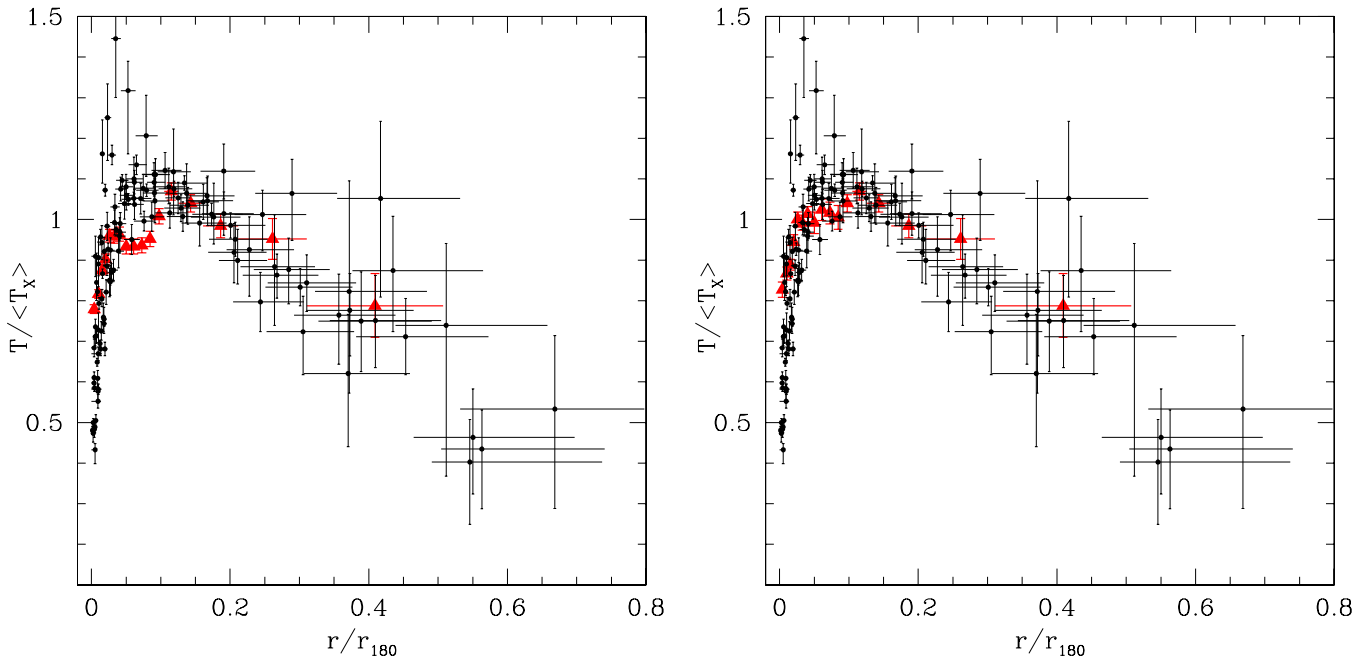
Figure 8. Left: temperature profile measured for Hydra A (red triangles, corresponding to the profile shown in the left panel of Figure 4) overlaid on the temperature profiles of a sample of 12 relaxed clusters presented by Vikhlinin et al. (2005). The temperatures are scaled to the cluster emission-weighted temperature excluding the central 70 kpc regions. By extracting the global spectrum of Hydra A, after masking the central 67″, we measured a value $\langle T_X \rangle = 3.76 \pm 0.03$ keV. The profiles for all clusters are projected and scaled in radial units of the virial radius r_{vir}, estimated from the relation $r_{vir} = 2.74\,\mathrm{Mpc}\sqrt{\langle T_X \rangle/10\,\mathrm{keV}}$ (Evrard et al. 1996). Right: similar to the left panel, but with the temperature profile measured for Hydra A after masking the cool filaments (corresponding to the profile shown in the right panel of Figure 4).

(A color version of this figure is available in the online journal.)

Table 5
Deprojection Analysis

Shell (″)	kT_{cool} (keV)	EM_{cool} ($\times 10^{-3}$)	kT_{hot} (keV)	EM_{hot} ($\times 10^{-3}$)	V_{tot} (cm^3)	f_{cool}	$n_{e,cool}$ (cm^{-3})	M_{cool} ($M_\odot$)	f_{hot}	$n_{e,hot}$ (cm^{-3})	M_{hot} ($M_\odot$)
Inner (0–72)	$1.77^{+0.13}_{-0.06}$	3.07	$4.01^{+0.04}_{-0.04}$	13.3	5.35×10^{70}	0.043	0.032	6.86×10^{10}	0.957	0.014	6.68×10^{11}
Middle (72–145)	$1.58^{+0.08}_{-0.10}$	1.64	$4.01^{+0.04}_{-0.04}$	10.9	3.85×10^{71}	0.023	0.012	9.90×10^{10}	0.977	0.0047	1.65×10^{12}
Outer (145–339)	. . .	0	$4.01^{+0.04}_{-0.04}$	12.5	5.20×10^{72}	0	0	0	1	0.0136	6.59×10^{12}

Notes. Results of the deprojection analysis in three concentric 360° annular regions (indicated in the first column) in the 0.5–8.0 keV energy range using the XSPEC `projct×wabs×(apec+apec)` model. The normalization of the cool component in the outer shell is fixed to zero, and the temperature values of the hot components are linked between all shells. The fit gives $\chi^2/\mathrm{dof} = 4993.5/2811$. The normalizations, $EM_{cool(hot)}$, are in XSPEC units of $10^{-14} n_{e,cool(hot)} n_p V_{cool(hot)}/4\pi [D_A(1+z)]^2$. Errors are at the 90% confidence levels on a single parameter of interest. The ratio of the relative volumes occupied is estimated as $V_{cool}/V_{hot} = (EM_{cool}/EM_{hot}) \cdot (kT_{cool}/kT_{hot})^2$, and the filling factor f is defined as $f_{cool(hot)} = V_{cool(hot)}/V_{tot}$, with $V_{tot} = V_{cool} + V_{hot}$. The masses are thus estimated from the relation: $M = \rho f V_{tot}$, where we use the conversion from electron number density to gas density $\rho = 1.83\,\mu n_e m_H$.

the corresponding pre-shock ones, although due to the large error bars, the pre-shock and post-shock temperatures are consistent.

6.2. Evidence for Gas Dredge-up along the Cool Filaments

The fact that the scaled temperature profile of Hydra A measured after masking the filaments agrees with the general shape of the temperature profiles observed for relaxed clusters (right panel of Figure 8) is a clear indication that these filaments are responsible for the plateau of cool gas. In Section 5, we performed a detailed (projected) spectral analysis and found evidence for multiphase gas, which may have been uplifted with the radio lobes, giving rise to the cooler filaments and plateau. In order to estimate the mass of the cool gas in the filaments, we must correct for the effects of projection along the line of sight. Starting from the annuli used to derive the

global temperature profile, we binned them together in order to obtain three shells suitable for a simple deprojection analysis of the cool filaments. In particular, using three annuli: inner (0″–72″ ∼ 0–76 kpc), middle (72″–145″ ∼ 76–152 kpc), and outer (145″–339″ ∼ 152–360 kpc), we performed a deprojection analysis of the absorbed 2T model with the XSPEC `projct` model. Under the assumption of spherical shells of emission, this model calculates the geometric weighting factors, according to which the emission is redistributed amongst the projected annuli. The outer shell was assumed to include only gas at the ambient temperature, which is linked to the temperature values of the hot components in the inner and middle shells. The detailed results of the deprojection analysis are shown in Table 5.

We found that the hot phase has a temperature of 4 keV, in agreement with the observed global temperature profile (Figure 4), and that the cool component is, on average, at
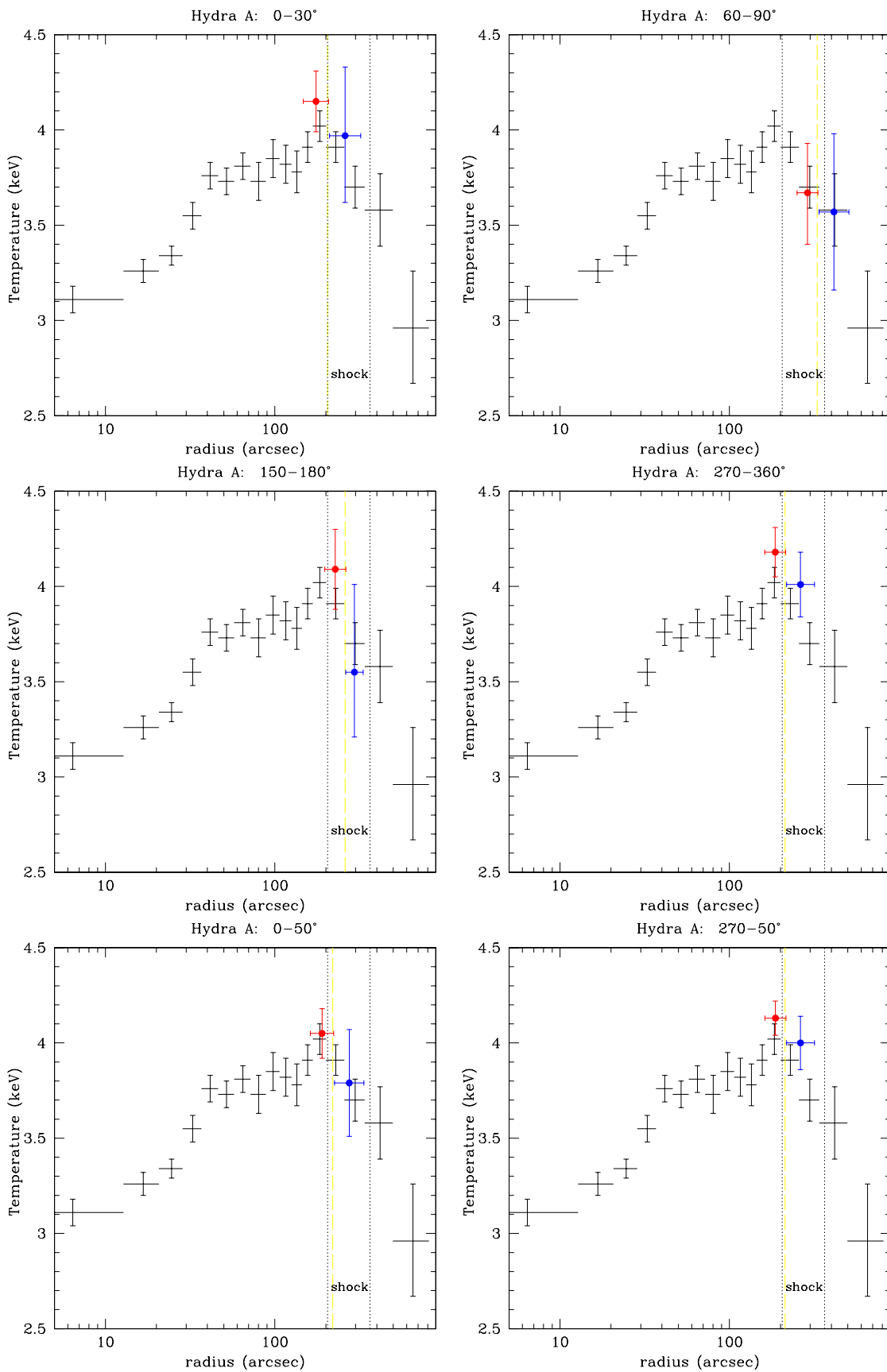
Figure 9. Temperatures measured in the pre-shock (blue) and post-shock (red) regions of some of the sectors shown in Figure 1. Radial error bars show the limits of the regions. The underlying global cluster profile, measured after masking the cool filaments corresponding to the profile shown in the right panel of Figure 4, is shown in black. The yellow dashed line indicates the radius of the shock front in each sector, while the dotted lines indicate the inner and outer radii of the shock front as determined in Section 3.1. The bottom panels are for binned sectors.

(A color version of this figure is available in the online journal.)

~1.6 keV. By taking into account the relative filling factor, f, calculated under the assumption that the two thermal components are in pressure equilibrium in each shell, in the middle shell we estimated a mass of cool gas of $9.9 \times 10^{10} M_\odot$ (and a mass of hot gas of $1.7 \times 10^{12} M_\odot$). We note that this estimate is considerably larger than the mass of cool gas reported by Simionescu et al. (2009b). The discrepancy between the two measurements can be ascribed to the fact that we included the mass content of the mushroom-cap (namely, sectors ENE, NNE, NNW in Figure 5). Using the entropy of the cooler phase and comparing to the entropy profile of the Hydra A cluster measured by David et al. (2001), we could estimate where it originated. From the density and temperature values measured in the middle shell (see Table 5), the cool gas has an entropy $S = kT_{cool} n_{e,cool}^{-2/3} \sim$ 30 keV cm^2. As shown by the profile of David et al. (2001), gas at such entropy is located around 30 kpc from the cluster center. Therefore, it is very likely that the cool gas, which is now observed in the filaments at ~75–150 kpc, was lifted from the central 30 kpc. In this case, the most obvious way to move the gas is by some form of entrainment or dredge up of cool material from the center of the cluster in the rising lobes. Churazov et al. (2000) have indeed shown that hot buoyant bubbles produced by the expanding central radio source can dredge up cool material from the center of the cluster. The mass of cool gas at ~75–150 kpc is $9.9 \times 10^{10} M_\odot$, which is ~60% of the total mass of gas remaining within 30 kpc ($1.7 \times 10^{11} M_\odot$; David et al. 2001). Assuming that such a mass was lifted out of the central 30 kpc by a continuous outflow or a series of bursts from the nucleus of the central galaxy over the past 200–500 Myr (which created the cavity system; Wise et al. 2007), it would amount to outflows of a few hundred $M_\odot$ yr^{-1}. There would thus be a development of a convectively unstable region that can significantly reduce the net inflow of cooling gas (see also David et al. 2001; Nulsen et al. 2002). Therefore, our results show that the AGN feedback in Hydra A is acting not only by directly re-heating the gas, but also by removing a substantial amount of potential fuel for the supermassive black hole.

The energy required to lift the cool gas gives a lower limit on the amount of AGN outburst energy deposited in the ICM. This value can be estimated by calculating the variation in gravitational potential energy during the lifting process. If we assume that the undisturbed ICM is approximately isothermal with sound speed $c_s \approx 1000$ km s^{-1} and is in a hydrostatic configuration with density profile $\rho(r)$, we can calculate this quantity as (Reynolds et al. 2008)

$$\Delta E = \frac{M_{cool} c_s^2}{\gamma} \ln \left(\frac{\rho_i}{\rho_f} \right), \qquad (1)$$

where M_{cool} is the lifted mass, ρ_i and ρ_f are the initial and final densities of the surrounding ICM, and $\gamma = 5/3$ is the ratio of specific heat capacities. From the density profile presented by David et al. (2001) we estimated that the energy required to lift the cool gas is $\gtrsim 2.2 \times 10^{60}$ erg. This value is comparable to the work required to inflate all of the cavities against the surrounding pressure (Wise et al. 2007) and is ~25% of the total energy of the large-scale shock (Nulsen et al. 2005). Although we find evidence for a more extended gas dredge-up than previously estimated, there is a remarkable correlation between the cool filaments studied here and the metal-rich filaments in the iron-abundance maps measured by Simionescu et al. (2009b) and Kirkpatrick et al. (2009). This is consistent with the idea that Hydra A's powerful radio source is able to

lift cool, metal-rich gas from the central region and distribute it throughout the X-ray atmosphere of the cluster. A similar effect is observed in M87 (Simionescu et al. 2008; Werner et al. 2010). We finally note that by summing our estimates of the integrated mass of cool gas, $M_{cool}(<152\,\text{kpc}) \sim 1.7 \times 10^{11} M_\odot$, and hot gas, $M_{hot}(<152\,\text{kpc}) \sim 2.3 \times 10^{12} M_\odot$, in the inner and middle shells we measure a total mass of gas $M_{gas}(<152\,\text{kpc}) \sim 2.5 \times 10^{12} M_\odot$ which is in agreement with the gas mass profile measured by David et al. (2001), so our general picture is self-consistent.

7. SUMMARY

The main results of this work can be summarized as follows.

1. We studied the azimuthal properties of the weak (Mach number ~1.2–1.3), large-scale shock and attempted to measure the temperature jump associated with the shock in different directions. The errors in the temperature measurements are too large to constrain the temperature jump caused by the shock. Furthermore, we note that the detection of a temperature rise in the regions immediately inside of the front is complicated by the underlying rising temperature profile of the cluster atmosphere.

2. Our detailed spectral analysis indicates the presence of multiphase gas along soft filaments seen in the hardness ratio map. The cooler gas has a significant impact on the radial temperature profile of the cluster. After correcting for the effect of the cool filaments, Hydra A's temperature profile is consistent with the form observed in relaxed galaxy clusters. Thus, it is unlikely that the observed temperature peak is produced by the shock.

3. The cool filaments are direct evidence for substantial dredge-up of low-entropy material by the rising lobes: ~60% of the gas mass remaining in the central 30 kpc has been lifted along the cool filaments to the observed current position of 75–150 kpc. The outflow amounts to a few hundred $M_\odot$ yr^{-1}, which is comparable to the inflow rate formerly estimated for the cooling flow. The energy required to lift the cool gas is ~25% of the total energy of the large-scale shock and is comparable to the work required to inflate the cavities.

REFERENCES

Anders, E., & Grevesse, N. 1989, Geochim. Cosmochim. Acta, 53, 197
Benson, A. J., Bower, R. G., Frenk, C. S., Lacey, C. G., Baugh, C. M., & Cole, S. 2003, ApJ, 599, 38
Bîrzan, L., McNamara, B. R., Nulsen, P. E. J., Carilli, C. L., & Wise, M. W. 2008, ApJ, 686, 859
Bîrzan, L., Rafferty, D. A., McNamara, B. R., Wise, M. W., & Nulsen, P. E. J. 2004, ApJ, 607, 800
Churazov, E., Forman, W., Jones, C., & Böhringer, H. 2000, A&A, 356, 788
David, L. P., Nulsen, P. E. J., McNamara, B. R., Forman, W. R., Jones, C., Ponman, T., Robertson, B., & Wise, M. W. 2001, ApJ, 557, 546

Dickey, J. M., & Lockman, F. J. 1990, ARA&A, 28, 215
Diehl, S., Li, H., Fryer, C., & Rafferty, D. 2008, ApJ, 687, 173
Evrard, A. E., Metzler, C. A., & Navarro, J. F. 1996, ApJ, 469, 494
Fabian, A. C., Sanders, J. S., Allen, S. W., Crawford, C. S., Iwasawa, K.,
    Johnstone, R. M., Schmidt, R. W., & Taylor, G. B. 2003, MNRAS, 344, L43
Gitti, M., McNamara, B. R., Nulsen, P. E. J., & Wise, M. W. 2007, ApJ, 660,
    1118
Kaastra, J. S., et al. 2004, A&A, 413, 415
Kirkpatrick, C. C., Gitti, M., Cavagnolo, K. W., McNamara, B. R., David, L. P.,
    Nulsen, P. E. J., & Wise, M. W. 2009, ApJ, 707, L69
Lane, W. M., Clarke, T. E., Taylor, G. B., Perley, R. A., & Kassim, N. E.
    2004, AJ, 127, 48
Magorrian, J., et al. 1998, AJ, 115, 2285
McNamara, B. R., & Nulsen, P. E. J. 2007, ARA&A, 45, 117
McNamara, B. R., et al. 2000, ApJ, 534, L138
Nulsen, P. E. J., David, L. P., McNamara, B. R., Jones, C., Forman, W. R., &
    Wise, M. W. 2002, ApJ, 568, 163
Nulsen, P. E. J., McNamara, B. R., Wise, M. W., & David, L. P. 2005, ApJ, 628,
    629

Peterson, J. R., & Fabian, A. C. 2006, Phys. Rep., 427, 1
Peterson, J. R., et al. 2003, ApJ, 590, 207
Rafferty, D., McNamara, B. R., Nulsen, P. E. J., & Wise, M. W. 2006, ApJ, 652,
    216
Reynolds, C. S., Casper, E. A., & Heinz, S. 2008, ApJ, 679, 1181
Simionescu, A., Roediger, E., Nulsen, P. E. J., Brüggen, M., Forman, W. R.,
    Böringer, H., Werner, N., & Finoguenov, A. 2009a, A&A, 495, 721
Simionescu, A., Werner, N., Böringer, H., Kaastra, J. S., Finoguenov, A.,
    Brüggen, M., & Nulsen, P. E. J. 2009b, A&A, 493, 409
Simionescu, A., Werner, N., Finoguenov, A., Böringer, H., & Brüggen, M. 2008,
    ApJ, 482, 97
Taylor, B. 1996, ApJ, 470, 394
Taylor, G. B., Perley, R. A., Inoue, M., Kato, T., Tabara, H., & Aizu, K.
    1990, ApJ, 360, 41
Vikhlinin, A., Markevitch, M., Murray, S. S., Jones, C., Forman, W., & Van
    Speybroeck, L. 2005, ApJ, 628, 655
Werner, N., et al. 2010, MNRAS, 407, 2063
Wise, M. W., McNamara, B. R., Nulsen, P. E. J., Houck, J. C., & David, L. P.
    2007, ApJ, 659, 1153